HYBRID FE/BI MODELING OF 3D DOUBLY PERIODIC STRUCTURES UTILIZING TRIANGULAR PRISMATIC ELEMENTS AND A MPIE FORMULATION ACCELERATED BY THE EWALD TRANSFORMATION

T. Eibert, J. Volakis,
D. Wilton and D. Jackson

Sanders, A Lockheed Martin Co.
95 Canal Street NCA1-6268
P.O. Box 868
Nashua, NH 030601-0868

April 1998

PROJECT INFORMATION

PROJECT TITLE:	Hybrid Finite Element Design Codes for the SERAT Array
REPORT TITLE:	Hybrid FE/BI Modeling of 3D Doubly Periodic Structures Utilizing Triangular Prismatic Elements and a MPIE Formulation Accelerated by the Ewald Transformation
U-M REPORT No.:	035067-9-T
CONTRACT START DATE:	October 1996
END DATE:	September 1998
DATE:	April 5, 1997
SPONSOR:	Roland Gilbert SANDERS, INC, A Lockheed Martin Co. MER 24-1583 PO Box 868 Nashua, NH 030601-0868 Phone: (603) 885-5861 Email: RGILBERT@mailgw.sanders.lockheed.com
SPONSOR CONTRACT No.:	P.O. QP2047
U-M PRINCIPAL INVESTIGATOR:	John L. Volakis EECS Dept. University of Michigan 1301 Beal Ave Ann Arbor, MI 48109-2122 Phone: (313) 764-0500 FAX: (313) 747-2106 volakis@umich.edu http://www-personal.engin.umich.edu/~volakis/
CONTRIBUTORS TO THIS REPORT:	T. Eibert(UM), J. Volakis(UM), D. Wilton(UH) and D. Jackson(UH)

Hybrid FE/BI Modeling of 3D Doubly Periodic Structures Utilizing Triangular Prismatic Elements and a MPIE Formulation Accelerated by the Ewald Transformation

Thomas F. Eibert and John L. Volakis

Radiation Laboratory, EECS Department

The University of Michigan, Ann Arbor, MI 48109-2122

Donald R. Wilton and David R. Jackson

Department of Electrical and Computer Engineering

University of Houston, TX 77204-4793

Abstract

In this paper, we present the formulation of a finite element/boundary integral method for the analysis of three–dimensional doubly periodic structures based on arbitrary non–orthogonal lattice configurations. The method starts from a functional description of the field problem where only a single unit cell of the array is considered. This unit cell is meshed with triangular prismatic volume elements and the electric field intensity is discretized with edge-based expansion functions. On the side walls of the unit cell, phase boundary conditions are employed to relate the fields on opposing walls of the unit cell. On the top and/or bottom unit-cell planar surfaces, the mesh is terminated using a mixed potential integral equation. The required space-domain periodic Green's function is calculated after applying the Ewald transformation to convert the slowly converging series representation into two quickly converging series. The method is validated for simple slot and strip frequency selective surfaces

as well as microstrip dipole arrays. More complex geometries being investigated are slot–coupled microstrip patches, photonic bandgap materials, and the so–called "artificial puck plate" frequency selective surface bandpass structure.

1 Introduction

By applying appropriate periodicity conditions, the computational domain of infinite periodic structures can be reduced down to a single unit cell. Previous analyses have mainly been restricted to the application of Floquet's theorem to construct periodic Green's functions in the context of integral equation formulations. An overview of techniques for the analysis of single–layer frequency selective surfaces (FSSs) based on spectral domain integral equation formulations is given in [1], together with a discussion of cascading approaches for multilayered structures. Further examples of spectral-domain formulations involving the analysis of multilayered planar structures like aperture coupled microstrip patches are described in [2, 3]. A difficulty with spectral-domain formulations of periodic Green's functions is the slow convergence of the Floquet-mode series. Therefore, acceleration techniques like the method of Singh as applied in [4] or Shanks transformation [5] must be used in conjunction with mixed potential integral equation (MPIE) formulations. An overview of acceleration techniques is given in [6]. Optimum convergence behavior can be obtained by applying the so–called Ewald transformation, which was suggested by P. P. Ewald in his thesis [7] and later extended to deal with skewed angled three–dimensional crystal lattices [8]. A numerical implementation of the Ewald transformation for two–dimensional lattices was described in [9]. In [10], the Ewald transformation was used to speed–up the analysis of doubly periodic arrays of rectangular apertures in metallic screens. In [11] a volume integral equation formulation for the analysis

of three–dimensional periodic structures embedded in multilayered media is described. However, this approach has difficulties in dealing with metallic structures. Also, the computational complexity can be large unless advantage is taken of the Toeplitz properties of the coupling matrices resulting from regular discretizations.

Fully three–dimensional modeling capabilities can be achieved by using hybrid finite element (FE) / boundary integral (BI) methods. For example, a two–dimensional FE/BI approach was suggested [12] for the analysis of plane-wave diffraction by arbitrary cross section gratings. Three–dimensional approaches for the analysis of doubly periodic structures are presented in [13, 14, 15]. Both of these methods are based on FE modeling employing tetrahedral meshes and spectral domain Floquet mode expansions of the BI fields.

In this paper, we propose a hybrid FE/BI method employing distorted triangular prismatic elements for volume tessellation and a MPIE formulation in the spatial domain for mesh truncation. The triangular prismatic elements provide full geometrical adaptability in the plane of the triangles and structured meshing along the depth of the cell. Because structured gridding is used for volume meshing, simple automatic mesh generation can be employed for the analysis of multilayered FSS structures. Thus, prismatic elements can allow for design studies since geometry meshing is accomplished by varying a few external parameters without a need to manually re–grid the geometry at each design iteration. Another important aspect of this paper is the use of the Ewald acceleration technique for evaluating the periodic Green's function.

In Section 2 the formulation of the method is given starting from a functional description of the field problem. The majority of this section is devoted to the FE implementation involving the phase boundary conditions as well as the BI formulation with the Ewald transformation. Section 3 shows results for a variety of periodic structures, including antenna arrays and

artificial dielectrics.

2 Formulation

2.1 Weak Formulation of the Field Problem

We consider the periodic structure illustrated in Fig. 1 for time harmonic electromagnetic fields (an $e^{j\omega t}$ time factor is assumed and suppressed throughout). The array is assumed to be periodic in the xy–plane and the (m,n) cell of the array is obtained by shifting the $(0,0)$ cell through the relation

$$\boldsymbol{\rho}_{mn} = m\,\boldsymbol{\rho}_a + n\,\boldsymbol{\rho}_b\,. \tag{1}$$

Here, $\boldsymbol{\rho}_a, \boldsymbol{\rho}_b$ are the lattice vectors parallel to the xy–plane. For periodic excitation of the array with a linear phase factor, the fields in the array obey the periodicity conditions

$$\begin{aligned} \boldsymbol{E}(\boldsymbol{r} + m\,\boldsymbol{\rho}_a + n\,\boldsymbol{\rho}_b) &= \boldsymbol{E}(\boldsymbol{r})\,\mathrm{e}^{-j\boldsymbol{k}_{t00}\cdot(m\,\boldsymbol{\rho}_a + n\,\boldsymbol{\rho}_b)}\,, \\ \boldsymbol{H}(\boldsymbol{r} + m\,\boldsymbol{\rho}_a + n\,\boldsymbol{\rho}_b) &= \boldsymbol{H}(\boldsymbol{r})\,\mathrm{e}^{-j\,\boldsymbol{k}_{t00}\cdot(m\,\boldsymbol{\rho}_a + n\,\boldsymbol{\rho}_b)} \end{aligned} \tag{2}$$

with

$$\boldsymbol{k}_{t00} = k_{x00}\,\hat{\boldsymbol{x}} + k_{y00}\,\hat{\boldsymbol{y}} = \pm(k_0 \sin\vartheta_0 \cos\varphi_0\,\hat{\boldsymbol{x}} + k_0 \sin\vartheta_0 \sin\varphi_0\,\hat{\boldsymbol{y}})\,. \tag{3}$$

In (3) k_0 is the wavenumber of free space and ϑ_0, φ_0 are the spherical coordinates corresponding to the scan angles of a phased array (positive sign) or the arrival angles of an incident plane wave (negative sign). The pertinent finite element functional is

$$\begin{aligned} F(\boldsymbol{E}_{ad}, \boldsymbol{E}) &= \iiint_V \left[\frac{1}{\mu_r}(\nabla \times \boldsymbol{E}_{ad}) \cdot (\nabla \times \boldsymbol{E}) - k_0^2\,\boldsymbol{E}_{ad} \cdot \boldsymbol{E} + jk_0 Z_0\,\boldsymbol{E}_{ad} \cdot \boldsymbol{J}^{int}\right] dv \\ &\quad + jk_0 Z_0 \iint_S \boldsymbol{E}_{ad} \cdot (\boldsymbol{H} \times \hat{\boldsymbol{n}})\,ds\,, \end{aligned} \tag{4}$$

where $\boldsymbol{E}_{ad}$ is the solution of the adjoint field problem, $\boldsymbol{J}^{int}$ denotes an excitation current within the FE domain, S represents the bounding surface of the FE domain, $\hat{\boldsymbol{n}}$ is the unit surface normal directed out of the FE domain, and Z_0 is the wave impedance of free–space. It is well known that $\boldsymbol{H} \times \hat{\boldsymbol{n}}$ in the surface integral of (4) must be replaced by an expression in terms of $\boldsymbol{E}$. This is the process of mesh truncation and as noted earlier the BI will be employed for this purpose. Restricting ourselves to planar surfaces (as is the case with most practical problems), the appropriate BI relation in MPIE form is given by

$$\boldsymbol{H} = -2j\frac{k_0}{Z_0}\left[\iint_S G(\boldsymbol{r},\boldsymbol{r}_s)\,(\boldsymbol{E}\times\hat{\boldsymbol{n}})\,ds + \frac{1}{k_0^2}\nabla\iint_S G(\boldsymbol{r},\boldsymbol{r}_s)\,\nabla'\cdot(\boldsymbol{E}\times\hat{\boldsymbol{n}})\,ds\right] + \boldsymbol{H}^{inc}, \quad (5)$$

where $G(\boldsymbol{r},\boldsymbol{r}_s) = \exp(-jk_0|\boldsymbol{r}-\boldsymbol{r}_s|)/(4\pi|\boldsymbol{r}-\boldsymbol{r}_s|)$ is the scalar free–space Green's function and $\boldsymbol{H}^{inc}$ is an incident wave in the presence of a metallic interface in S. Substituting (5) into (4) and invoking the divergence theorem results in

$$\begin{aligned} F(\boldsymbol{E}_{ad},\boldsymbol{E}) \;=\; & \iiint_V \left[\frac{1}{\mu_r}(\nabla\times\boldsymbol{E}_{ad})\cdot(\nabla\times\boldsymbol{E}) - k_0^2\,\boldsymbol{E}_{ad}\cdot\boldsymbol{E} + jk_0Z_0\,\boldsymbol{E}_{ad}\cdot\boldsymbol{J}^{int}\right] dv \\ & -2k_0^2\left[\iint_S\iint_S G(\boldsymbol{r},\boldsymbol{r}_s)(\hat{\boldsymbol{n}}\times\boldsymbol{E}_{ad}(\boldsymbol{r}))\cdot(\hat{\boldsymbol{n}}\times\boldsymbol{E}(\boldsymbol{r}_s))\,ds_s ds\right. \\ & \left. -\frac{1}{k_0^2}\iint_S\iint_S G(\boldsymbol{r},\boldsymbol{r}_s)\,\nabla\cdot(\hat{\boldsymbol{n}}\times\boldsymbol{E}_{ad}(\boldsymbol{r}))\,\nabla_s\cdot(\hat{\boldsymbol{n}}\times\boldsymbol{E}(\boldsymbol{r}_s))\,ds_s ds\right] \\ & +j\,k_0Z_0\iint_S(\hat{\boldsymbol{n}}\times\boldsymbol{E}_{ad}(\boldsymbol{r}))\cdot\boldsymbol{H}^{inc}(\boldsymbol{r})\,ds\,, \end{aligned} \quad (6)$$

which is the exact functional description of the periodic field problem. Based on the periodicity condition (2), the solution domain can be restricted to a single unit cell of the periodic array. However, by this procedure additional (vertical) boundaries of the solution domain are created. The phase boundary conditions (PBCs), (2), must be employed on these to obtain the unique solution of the field problem. Moreover, the free–space Green's function $G(\boldsymbol{r},\boldsymbol{r}_s)$ must be replaced by the appropriate Green's function $G_p(\boldsymbol{r},\boldsymbol{r}_s)$ for a periodic array of δ–sources in free space.

2.2 Finite Elements

For the discretization of the volume integrals in (6) we employ edge–based basis functions on triangular prismatic elements as described in [16]. The resulting meshes give full modeling flexibility in the transverse direction but are structured in the direction normal to the triangular cross sections. Therefore, mesh generation with triangular prisms is much simpler in comparison to tetrahedral meshes and well–suited for designing layered periodic structures. As an example, a simplified FE mesh with triangular prisms for a unit cell of the infinite periodic array is illustrated in Fig. 2. The four vertical walls of the FE mesh are designated as $\Gamma_{le}, \Gamma_{ri}, \Gamma_{lo}, \Gamma_{up}$, where Γ_{le} and Γ_{lo} are assumed to be the sidewalls opposite to Γ_{ri} and Γ_{up}, respectively. A possible imposition of the PBCs on the vertical walls of the FE mesh was discussed in detail in [14] and [15]. The basic observation in this context is that the fields on a vertical boundary of the FE mesh are related to the fields on the opposite boundary by (2) through a phase relation. If e_m is the unknown field at an edge on one of the vertical walls, the value e_n of the field at the corresponding edge on the opposite sidewall is given by

$$e_n = e_m \, \mathrm{e}^{-j\boldsymbol{k}_{t00}\cdot\Delta\boldsymbol{r}} , \tag{7}$$

where $\Delta\boldsymbol{r}(= \boldsymbol{\rho}_a$ or $\boldsymbol{\rho}_b)$ is the vector joining the two edges. This relation requires that the surface meshes of the opposite vertical walls be identical and this is easily satisfied using prismatic meshes but not so easily using tetrahedral meshes. In our implementation, we eliminate the unknowns on the surfaces Γ_{ri} and Γ_{up} by relating them to those on Γ_{le} and Γ_{lo} using (7). For example, in Fig. 2 the unknown field at edge n_{up} is replaced by the unknown field at edge n_{lo}. Similarly, the unknown field at edge m_{ri} is replaced by the unknown field at edge m_{le}. For the construction of the FE system matrix, this means that the corresponding matrix elements are modified and condensed according to (7) as described in [14, 15]. However,

in our implementation, matrix condensation is performed during the generation of the matrix and not as a second step. This allows for the most efficient sparse matrix storage.

2.3 Boundary Integral

The edge–based basis functions for triangular prisms reduce to Rao-Wilton-Glisson basis functions [17] on the top and bottom triangular surface meshes of the periodic unit cell. Therefore, these basis functions are used to represent the field in the boundary integral in (6). In the spatial domain, the periodic Green's function $G_p(\boldsymbol{r}, \boldsymbol{r}_s)$ has the form

$$G_p(\boldsymbol{r}, \boldsymbol{r}_s) = \sum_{m=-\infty}^{\infty} \sum_{n=-\infty}^{\infty} \mathrm{e}^{-j\boldsymbol{k}_{t00}\cdot\boldsymbol{\rho}_{mn}} \frac{\mathrm{e}^{-jk_0 R_{mn}}}{4\pi R_{mn}}, \tag{8}$$

where

$$R_{mn} = |\boldsymbol{r} - \boldsymbol{r}_s - \boldsymbol{\rho}_{mn}|\,. \tag{9}$$

In the spectral domain, $G_p(\boldsymbol{r}, \boldsymbol{r}_s)$ becomes

$$G_p(\boldsymbol{r}, \boldsymbol{r}_s) = \frac{1}{A} \sum_{m=-\infty}^{\infty} \sum_{n=-\infty}^{\infty} \frac{1}{2jk_{zmn}} \mathrm{e}^{-j\boldsymbol{k}_{tmn}\cdot(\boldsymbol{\rho}-\boldsymbol{\rho}_s)} \mathrm{e}^{-jk_{zmn}|z-z_s|}, \tag{10}$$

where $A = |\boldsymbol{\rho}_a \times \boldsymbol{\rho}_b|$ is the cross sectional area of the unit cell,

$$\boldsymbol{r} = \boldsymbol{\rho} + z\,\hat{\boldsymbol{z}}, \tag{11}$$

$$\boldsymbol{k}_{tmn} = \boldsymbol{k}_{t00} + \frac{2\pi}{A}\left[m(\hat{\boldsymbol{z}} \times \boldsymbol{\rho}_a) + n(\boldsymbol{\rho}_b \times \hat{\boldsymbol{z}})\right] \tag{12}$$

is the so-called reciprocal lattice vector, and

$$k_{zmn} = \sqrt{k_0^2 - \boldsymbol{k}_{tmn} \cdot \boldsymbol{k}_{tmn}}, \tag{13}$$

where $\mathrm{Re}(k_{zmn}) \geq 0, \mathrm{Im}(k_{zmn}) \leq 0$. In many cases, the spectral domain representation (10) has satisfactory convergence behavior if applied in a spectral-domain formulation of the integral equation. However, for arbitrary array configurations analyzed in the space domain,

having strongly as well as weakly coupled array elements, it is necessary to have a representation that converges faster than either (8) or (10). This can be achieved by employing the so–called Ewald transformation originally proposed by Ewald for modeling optical and electrostatic potentials in three–dimensional ion lattices [8]. An application of the Ewald transformation for time harmonic fields of two–dimensional lattices was presented in [9]. The formulation in [9] is restricted to rectangular lattices, but Ewald's transformation is also applicable to skewed lattices by employing the reciprocal lattice representation used here. The Ewald transformation starts from the spatial domain representation of the periodic Green's function (8) and makes use of the identity

$$\frac{e^{-jk_0R_{mn}}}{R_{mn}} = \frac{2}{\sqrt{\pi}}\int_0^\infty e^{-R_{mn}^2s^2+\frac{k_0^2}{4s^2}}\,ds, \tag{14}$$

where s is a complex variable. In order that the integrand remain bounded as $s \to 0$ and $s \to \infty$, it is sufficient to choose the path such that $\arg(s) = \frac{\pi}{4}$ at the endpoints. Next, (14) is substituted into (8) and the parameter E is introduced to split the integral into two terms, as

$$G_p(\boldsymbol{r},\boldsymbol{r}_s) = G_{p1}(\boldsymbol{r},\boldsymbol{r}_s) + G_{p2}(\boldsymbol{r},\boldsymbol{r}_s) \tag{15}$$

where

$$G_{p1}(\boldsymbol{r},\boldsymbol{r}_s) = \frac{1}{4\pi}\sum_{m=-\infty}^{\infty}\sum_{n=-\infty}^{\infty} \mathrm{e}^{-j\boldsymbol{k}_{t00}\cdot\boldsymbol{\rho}_{mn}}\,\frac{2}{\sqrt{\pi}}\int_0^E \mathrm{e}^{-R_{mn}^2s^2+\frac{k_0^2}{4s^2}}\,ds\,, \tag{16}$$

$$G_{p2}(\boldsymbol{r},\boldsymbol{r}_s) = \frac{1}{4\pi}\sum_{m=-\infty}^{\infty}\sum_{n=-\infty}^{\infty} \mathrm{e}^{-j\boldsymbol{k}_{t00}\cdot\boldsymbol{\rho}_{mn}}\,\frac{2}{\sqrt{\pi}}\int_E^\infty \mathrm{e}^{-R_{mn}^2s^2+\frac{k_0^2}{4s^2}}\,ds\,. \tag{17}$$

Using the identity [18] (Eq. 7.4.34)

$$\frac{2}{\sqrt{\pi}}\int_E^\infty \mathrm{e}^{-R_{mn}^2s^2+\frac{k_0^2}{4s^2}}\,ds = \frac{1}{2R_{mn}}\left[\mathrm{e}^{-jk_0R_{mn}}\,\mathrm{erfc}\left(R_{mn}E-\frac{jk}{2E}\right) + \mathrm{e}^{jk_0R_{mn}}\,\mathrm{erfc}\left(R_{mn}E+\frac{jk}{2E}\right)\right], \tag{18}$$

where erfc is the complementary error function, $G_{p2}(\boldsymbol{r}, \boldsymbol{r}_s)$ can be written as

$$G_{p2}(\boldsymbol{r}, \boldsymbol{r}_s) = \sum_{m=-\infty}^{\infty} \sum_{n=-\infty}^{\infty} \frac{\mathrm{e}^{-j\boldsymbol{k}_{t00}\cdot\boldsymbol{\rho}_{mn}}}{8\pi R_{mn}} \left[\mathrm{e}^{-jk_0 R_{mn}} \operatorname{erfc}\left(R_{mn}E - \frac{jk}{2E}\right) + \mathrm{e}^{jk_0 R_{mn}} \operatorname{erfc}\left(R_{mn}E + \frac{jk}{2E}\right)\right], \tag{19}$$

which is a "modified" spatial domain portion of the periodic Green's function. Making use of the Poisson transformation, or alternatively following the procedure in [8, 9] employing a transformation formula for the series expansion of the ϑ-function, (16) finally is transformed to

$$G_{p1}(\boldsymbol{r}, \boldsymbol{r}_s) = \frac{1}{A} \sum_{m=-\infty}^{\infty} \sum_{n=-\infty}^{\infty} \frac{1}{4jk_{zmn}} \mathrm{e}^{-j\boldsymbol{k}_{tmn}\cdot(\boldsymbol{\rho}-\boldsymbol{\rho}_s)} \left[\mathrm{e}^{-jk_{zmn}|z-z_s|} \operatorname{erfc}\left(\frac{jk_{zmn}}{2E} - |z-z_s|E\right) + \mathrm{e}^{jk_{zmn}|z-z_s|} \operatorname{erfc}\left(\frac{jk_{zmn}}{2E} + |z-z_s|E\right)\right], \tag{20}$$

which can be identified as a "modified" spectral domain portion of the periodic Green's function. For planar BI surfaces, we can select $z = z_s = 0$, giving the simplified form

$$G_{p1}(\boldsymbol{r}, \boldsymbol{r}_s) = \frac{1}{A} \sum_{m=-\infty}^{\infty} \sum_{n=-\infty}^{\infty} \frac{1}{2jk_{zmn}} \mathrm{e}^{-j\boldsymbol{k}_{tmn}\cdot(\boldsymbol{\rho}-\boldsymbol{\rho}_s)} \operatorname{erfc}\left(\frac{jk_{zmn}}{2E}\right). \tag{21}$$

The two expressions (19) and (20) or (21) both converge exponentially (Gaussian convergence) and their computation is therefore very efficient requiring only a few terms of the series. The parameter E controls the convergence rate. As E becomes larger, the spatial series (19) converges faster, while the spectral series (20) or (21) converges slower. The optimum parameter is that which makes the two series converge at the same rate, so that equal numbers of terms are required in the calculation of both series (assuming that the calculation time for each term in the two series is the same). By analysis of the asymptotic behavior of the series terms, the optimum parameter E_{opt} is found to be [9]

$$E_{opt} = \sqrt{\frac{\pi}{A}}. \tag{22}$$

Choosing this value for E and adjusting the summation limits so that the most dominant terms are kept, in almost all practical cases it is sufficient to include only 9 summation terms in (19) and (20) or (21) (i.e., the summation limits are from –1 to +1), in which case the error level usually is less than 0.1%.

For the implementation of the BI portion of the method, we apply the same phase transformations to the matrix elements associated with edges on Γ_{ri} and Γ_{up} (see Fig. 2) as done in the FE portion of the implementation (see subsection 2.2). This is in contrast to the concept of "overlapping elements" described in [12, 14, 15]. However, it is advantageous for our spatial-domain MPIE formulation for treating the singularities of the Green's function. For our approach, source and test triangles are always inside the unit cell and it is therefore guaranteed that the singularities of the neighboring array cells are never inside the test triangle. Nevertheless, it is still necessary to carefully deal with the singularities of the neighboring array elements that are close to the test triangles, as illustrated in Fig. 3. The singularities, especially those of the self–cell elements, can be integrated using the formulas given in [19, 20].

3 Results

For the validation of the method, we first analyzed the two simple FSS structures illustrated in Figs. 4 and 5. These were originally considered in [1]. The example in Fig. 4 is a slot FSS on a dielectric slab where the BI on the top surface is restricted to the slot aperture. In the diagram, we give the computed power reflection coefficient of the infinite slot array for an incident TM plane wave. A method of moments (MoM) formulation employing a multilayered Green's function was also developed during this study and is used to compare results for this and several other cases presented here. The FE/BI results were obtained using 4 subdivisions

along the width of the slot and 15 subdivisions along the length of the slot. As seen, the results in Fig. 4 agree almost exactly with the MoM data. Compared to the results presented in [1], both curves are slightly shifted to higher frequencies. The structure illustrated in Fig. 5 is a strip dipole FSS embedded in a dielectric layer. Again, our FE/BI results for the power reflection coefficient are compared to the corresponding results based on the MoM code for planar structures. In this case, the incident plane wave was TE polarized, parallel to the orientation of the strip dipoles. In contrast to the case of the slot array, the two resonance curves for the strip dipole array show a slight frequency shift of about 1%. We note that the FE/BI results were obtained using 16 subdivisons along the length and 8 subdivisions along the width of the strip dipole. Further increases in the sampling rate showed that the results were converged. In Fig. 6 the active reflection coeffecient for a microstrip dipole array is depicted to demonstrate the antenna and scan modeling capabilities of our FE/BI method. The results compare very well to our own MoM results and those of [22].

A more complex FSS structure consisting of two slot coupled microstrip patches [2] is given in Fig. 7. The modeling of this structure using MoM-based integral equation analysis is challenging, involving electric and magnetic surface current densities in layered media. However, modeling of the cell in Fig. 7 is a routine task in the FE/BI implementation. First, the geometric dimensions of the structure in Fig. 7 were designed to get a transmission coefficient curve with two separated resonance peaks as shown in Fig. 8. In [2], MoM results were compared to measurements; however, the measured resonance curves were obtained for a slot length of 12 mm whereas in the simulation a slot length of 11.2 mm was used to match the results. In our FE/BI simulations we found a good match of the resonance curves using the original slot length of 12 mm. However, discrepancies between the two curves are obvious in the range between the two resonances. For the results shown in Fig. 9, the geometric dimensions were

selected to obtain bandpass behavior of the transmission coefficient curve. Again, our FE/BI results are compared to MoM calculations as well as to measurements published in [2]. The FE/BI calculations were performed for a slot length of 9 mm in contrast to 8 mm used to obtain the computed and measured results in [2]. ¿From the curves it can be seen that the FE/BI results give smaller values for the transmission coefficient in the passband region of the filter. On the other side the MoM values in this range are a little bit too large compared to the measured results but overall they fit better than the FE/BI results.

As another example we consider the dielectric slab in Fig. 10 with embedded periodic material blocks. These lattices are often referred to as photonic bandgap materials. The diagram in Fig. 10 shows the reflection coefficient of plane waves incident on the slab with different incidence angles. The reflection coefficient curves exhibit the typical resonances of photonic bandgap materials. Compared to calculations obtained by a volume integral equation method [11], the first resonance is slightly shifted to a lower frequency whereas the frequency shift for the second resonance is larger. For TM–waves with oblique incidence, the resonances shift to higher frequencies and this is in agreement with [11].

As a final example, Fig. 11 shows the unit cell for a so–called "artificial puck plate" FSS screen which was presented in [23] and analyzed in [13]. The basic FSS element is a dielectric-filled cylindrical waveguide with metallic walls and circular metallic irises in its apertures. On the top and bottom of the metallic plate, dielectric layers are placed for the optimization of the frequency behavior of the bandpass structure. The surface mesh used to grow the prismatic volume mesh of the unit cell is shown in Fig. 12. Our calculations are given in Fig. 13 and are compared to MoM data and FE/BI results based on a tetrahedral mesh published in [13]. As can be seen, our FE/BI curves are closer to the MoM curves than the FE/BI results from [13]. This is likely due to our higher sampling rate.

4 Conclusion

In this paper, we presented a hybrid FE/BI method for the analysis of 3D doubly periodic structures. The method can handle non–orthogonal lattices as well as arbitrary scan directions. The FE portion of the approach utilizes triangular prismatic volume meshes with edge-based basis functions for the electric field intensity. This meshing strategy provides for geometrical flexibility and ease of mesh generation for layered structures. On the top and/or bottom boundary planes of the unit cell, the mesh was truncated by a boundary integral and a periodic phase boundary condition was employed on the side walls of the unit cell mesh. The BI was implemented in MPIE formulation with the periodic Green's function in the space domain being computed using the Ewald acceleration technique, resulting in very fast convergence of the series representation. The method was validated for simple slot and strip FSS as well as for microstrip dipole antenna arrays. Further results were shown for slot-coupled microstrip patches, photonic bandgap arrays, and a bandpass FSS based on a circular hollow waveguide with dielectric cover layers.

Acknowledgements

This work was supported in part by the Office of Naval Research (ONR–313) through the Naval Air Warfare Center Aircraft Division (NAWCAD 4.5.5.5) contract with Sanders, A Lockheed Martin Corporation.

The first author acknowledges the fellowship support from the "German Academic Exchange Service (DAAD)".

References

[1] R. Mittra, C. H. Chan, T. Cwik, Techniques for Analyzing Frequency Selective Surfaces — A Review, *Proc. IEEE*, Vol. 76, No. 12, pp. 1593–1615, Dec. 1988.

[2] R. Pous, D. M. Pozar, A Frequency-Selective Surface Using Aperture-Coupled Microstrip Patches, *IEEE Trans. AP*, Vol. 39, No. 12, pp. 1763–1769, Dec. 1991.

[3] H. Aroudaki, V. Hansen, H.–P. Gemünd, E. Kreysa, Analysis of Low–Pass Filters Consisting of Multiple Stacked FSS's of Different Periodicities with Applications in the Submillimeter Radioastronomy, *IEEE Trans. AP*, Vol. 43, No. 12, pp. 1486–1491, Dec. 1995.

[4] R. M. Shubair, Y. L. Chow, Efficient Computation of the Periodic Green's Function in Layered Dielectric Media, *IEEE Trans. AP*, Vol. 41, No. 3, pp. 498–502, March 1993.

[5] R. A. Kipp, C. H. Chan, A Numerically Efficient Technique for the Method of Moments Solution for Periodic Structures in Layered Media, *IEEE Trans. MTT*, Vol. 42, No. 4, pp. 635–643, April 1994.

[6] N. Kınayman, M. I. Aksun, Comparative Study of Acceleration Techniques for Integrals and Series in Electromagnetic Problems, *Radio Science*, Vol. 30, No. 6, pp. 1713–1722, Nov./Dec. 1995.

[7] P. P. Ewald, *Dispersion und Doppelbrechung von Elektronengittern (Kristallen)*, Dissertation, München, 1912, (also *Ann. Phys. 49*, p. 1, 1916).

[8] P. P. Ewald, Die Berechnung optischer und elektrostatischer Gitterpotentiale, *Ann. Phys. 64*, pp. 253–287, 1921.

[9] K. E. Jordan, G. R. Richter, P. Sheng, An Efficient Numerical Evaluation of the Green's Function for the Helmholtz Operator on Periodic Structures, *J. of Comp. Phy.*, 63, pp. 222–235, 1986.

[10] A. W. Mathis, A. F. Peterson, Efficient Electromagnetic Analysis of a Doubly Infinite Array of Rectangular Apertures, *IEEE Trans. MTT*, Vol. 46, No. 1, pp. 46–54, Jan. 1998.

[11] H.–Y. D. Yang, R. Diaz, N. G. Alexopoulos, Reflection and Transmission of Waves from Multilayer Structures with Planar Implanted Periodic Material Blocks, *J. of the Opt. Soc. of Am., B*, Vol. 14, No. 10, pp. 2513–2521, Oct. 1997.

[12] S. D. Gedney, J. F. Lee, R. Mittra, A Combined FEM/MOM Approach to Analyze the Plane Wave Diffraction by Arbitrary Gratings, *IEEE Trans MTT*, Vol. 40, No. 2, pp. 363–370, Feb. 1992.

[13] E. W. Lucas, T. W. Fontana, A 3-D Hybrid Finite Element/Boundary Element Method for the Unified Radiation and Scattering Analysis of General Infinite Periodic Arrays, *IEEE Trans. AP*, Vol. 43, No. 2, pp. 145–153, Feb. 1995.

[14] D. T. McGrath, V. P. Pyati, Phased Array Antenna Analysis with the Hybrid Finite Element Method, *IEEE Trans. AP*, Vol. 42, No. 12, pp. 1625–1630, Dec. 1994.

[15] D. T. McGrath, V. P. Pyati, Periodic Structure Analysis Using a Hybrid Finite Element Method, *Radio Science*, Vol. 31, No. 5, pp. 1173–1179, Sep/Oct. 1996.

[16] T. Özdemir, J. L. Volakis, Triangular Prisms for Edge–Based Vector Finite Element Analysis of Conformal Antennas, *IEEE Trans. AP*, Vol. 45, No. 5, pp. 788–797, May 1997.

[17] S. M. Rao, D. R. Wilton, A. W. Glisson, Electromagnetic Scattering by Surfaces of Arbitrary Shape, *IEEE Trans. AP*, Vol. 30, No. 3, pp. 409–418, May 1982.

[18] M. Abramovitz, I. A. Stegun, *Handbook of Mathematical Functions*, Dover Publications, New York, 1965.

[19] D. R. Wilton, S. M. Rao, A. W. Glisson, D. H. Schaubert, O. M. Al-Bundak, C. M. Butler, Potential Integrals for Uniform and Linear Source Distributions on Polygonal and Polyhedral Domains, *IEEE Trans. AP*, Vol. 32, No. 3, pp. 276–281, March 19984.

[20] T. F. Eibert, V. Hansen, On the Calculation of Potential Integrals for Linear Source Distributions on Triangular Domains, *IEEE Trans. AP*, Vol. 43, No. 12, pp. 1499–1502, Dec. 1995.

[21] J. C. Vardaxoglou, A. Hossainzadeh, A. Stylianou, Scattering from Two-Layer FSS with Dissimilar Lattice Geometries, *IEE Proc. H*, Vol. 140, No. 1, pp. 59–61, Feb. 1993.

[22] D. M. Pozar, The Active Element Pattern, IEEE Trans. AP, Vol. 42, No. 8, pp. 1176–1178, Aug. 1994.

[23] R. G. Schmier, The Artificial Puck Frequency Selective Surface, URSI Radio Science Meeting, p. 266, Ann Arbor, 1993.

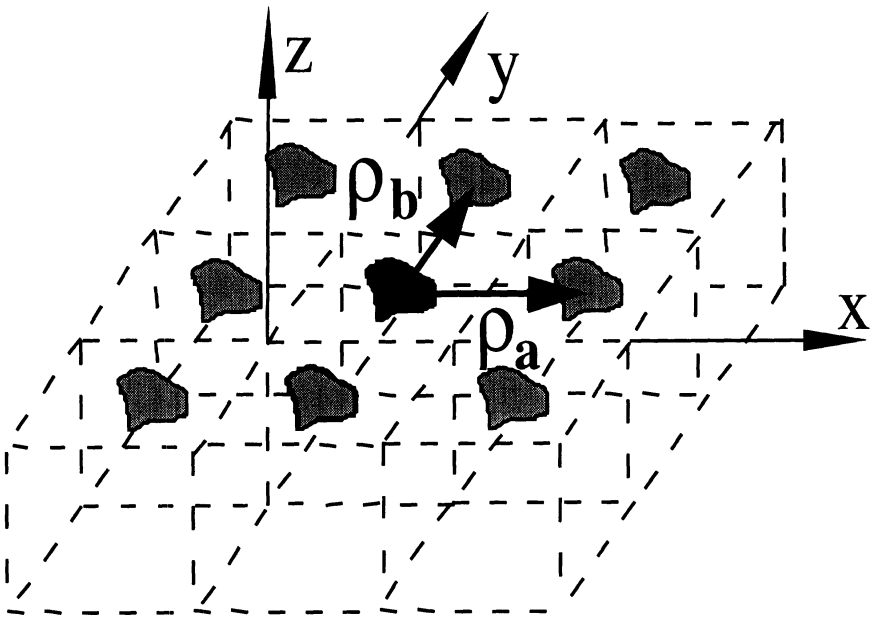

Figure 1: Infinite periodic structure

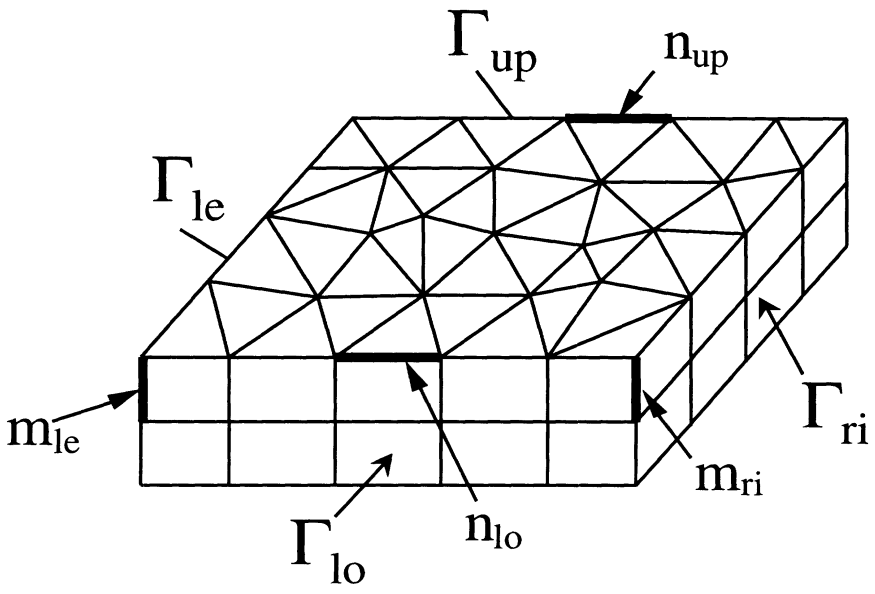

Figure 2: FE mesh consisting of triangular prisms

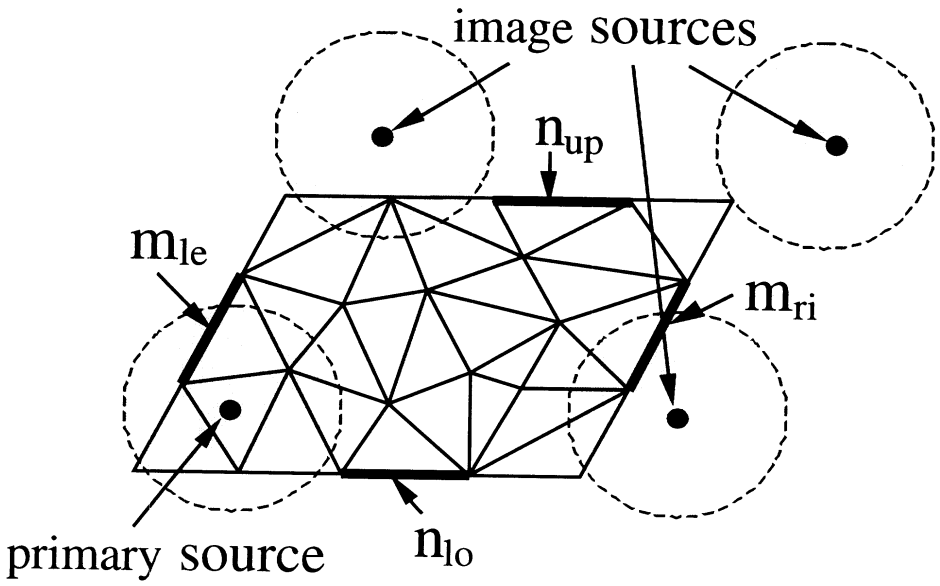

Figure 3: Periodic image sources in triangular BI mesh

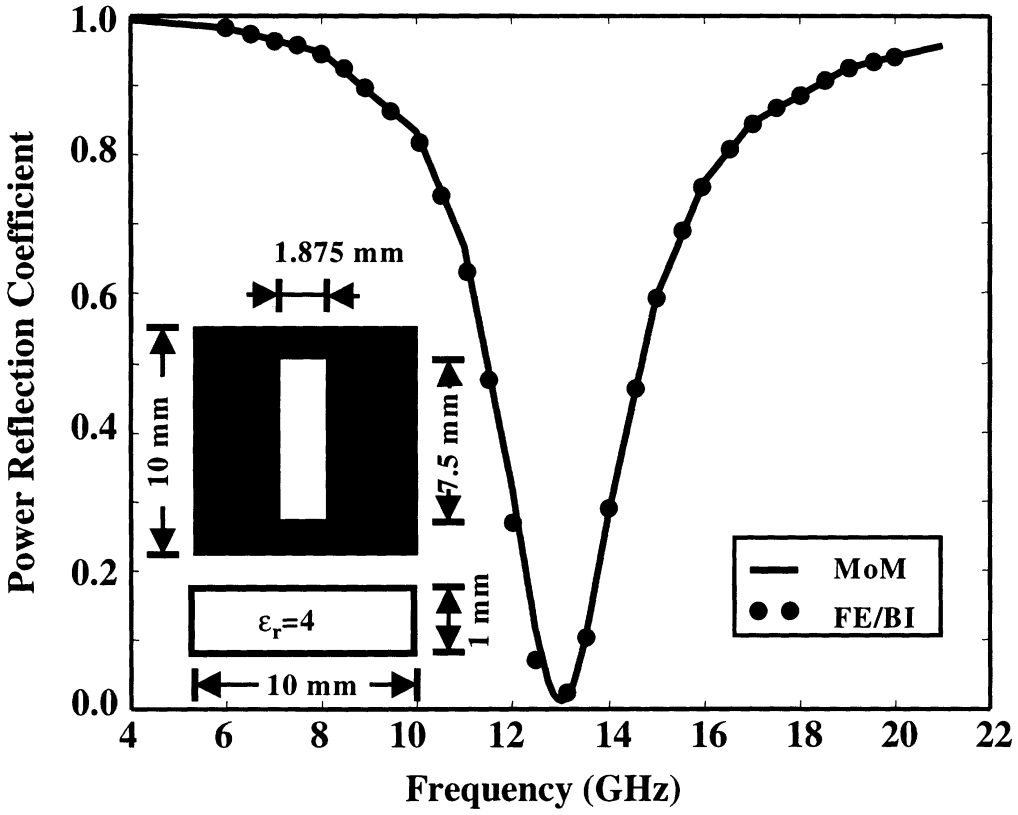

Figure 4: Power reflection from a 1–layer slot array for a plane wave (TM, $\vartheta_0 = 0.1^o, \varphi_0 = 0^o$)

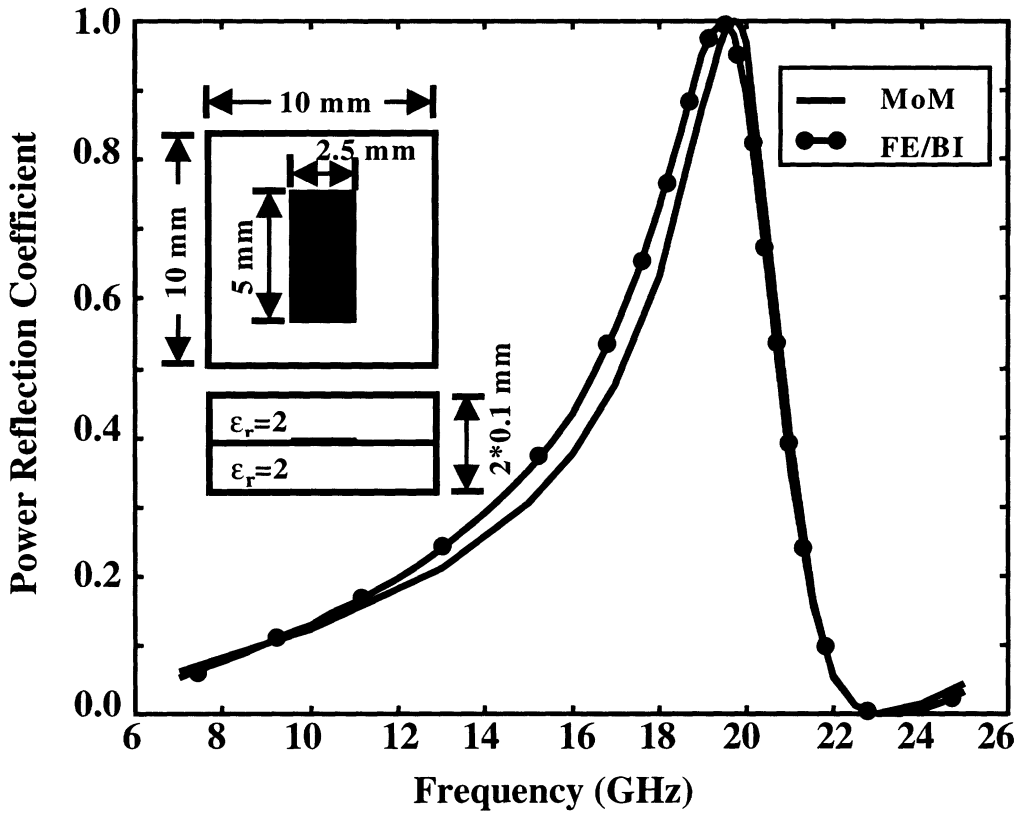

Figure 5: Power reflection from a 1–layer strip array for a plane wave (TE, $\vartheta_0 = 0.1^o, \varphi_0 = 0^o$)

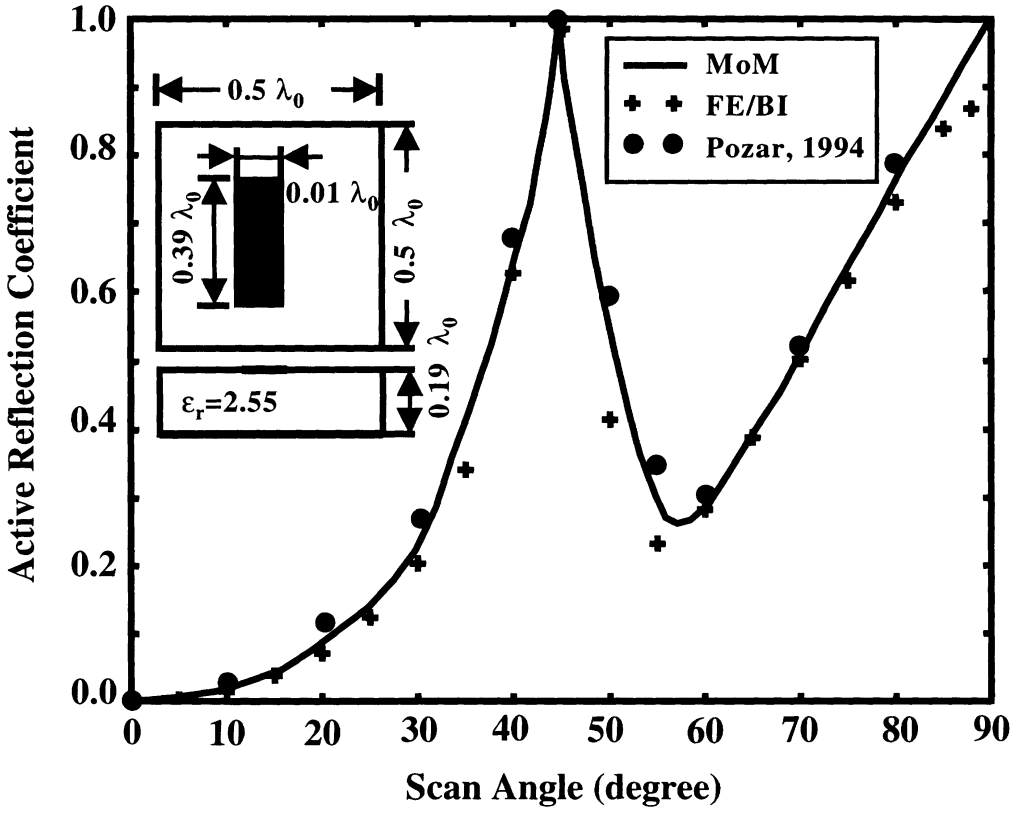

Figure 6: Active reflection coefficient for a microstrip dipole array as presented in [22], (TE, $\vartheta_0 = 0.1^o, \varphi_0 = 0^o$)

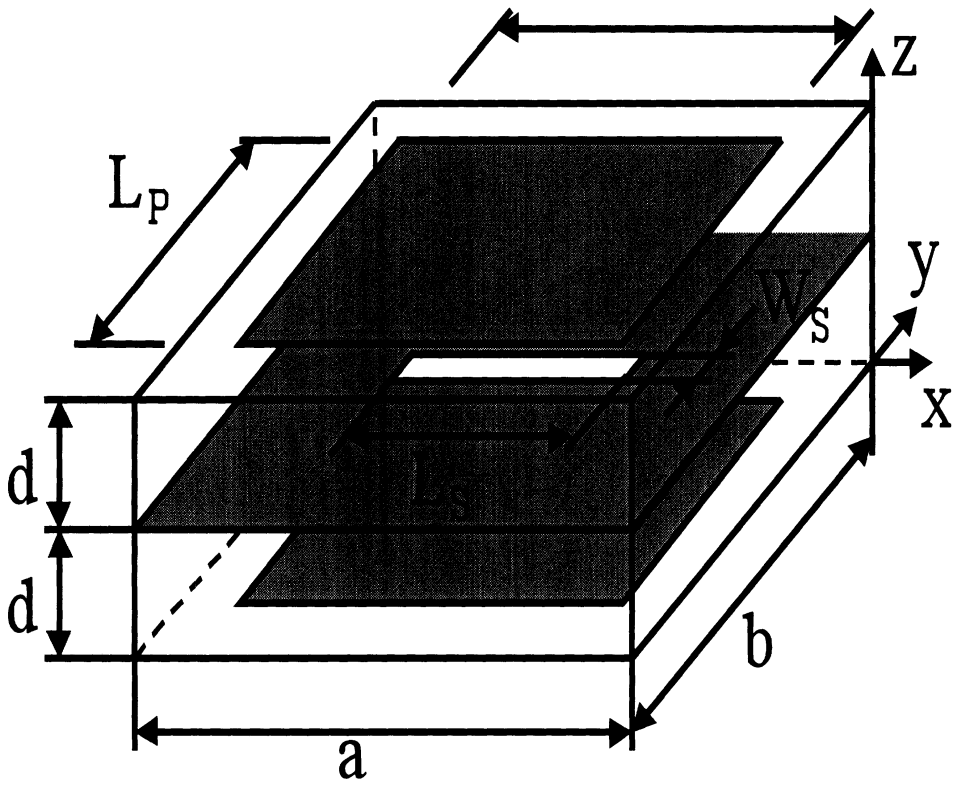

Figure 7: FSS unit cell of aperture coupled microstrip patches as suggested in [2], $\varepsilon_r = 2.2$, $d = 1.6$ mm, $a = 36.07$ mm, $b = 34.04$ mm.

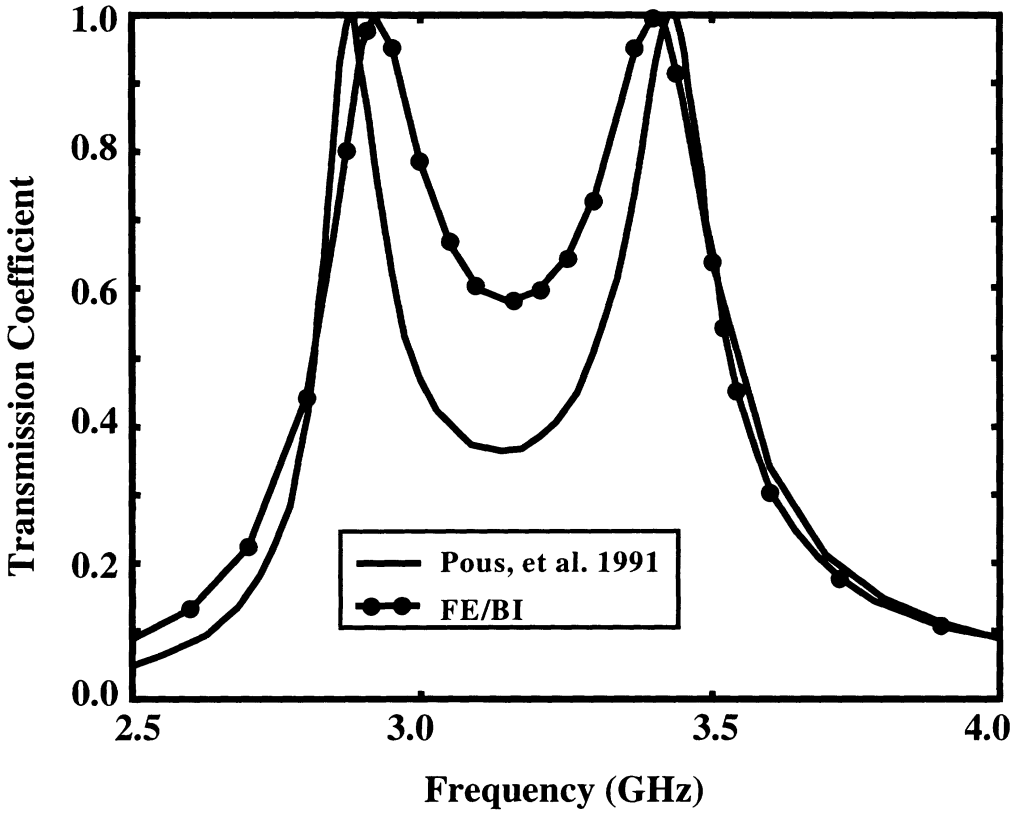

Figure 8: Transmission coefficient for the FSS structure in Fig. 7 compared to reference values from [2], $L_s = 12$ mm, $W_s = 2$ mm, $W_p = 28$ mm, $L_p = 18$ mm, (TM, $\vartheta_0 = 0.1^o, \varphi_0 = 0^o$).

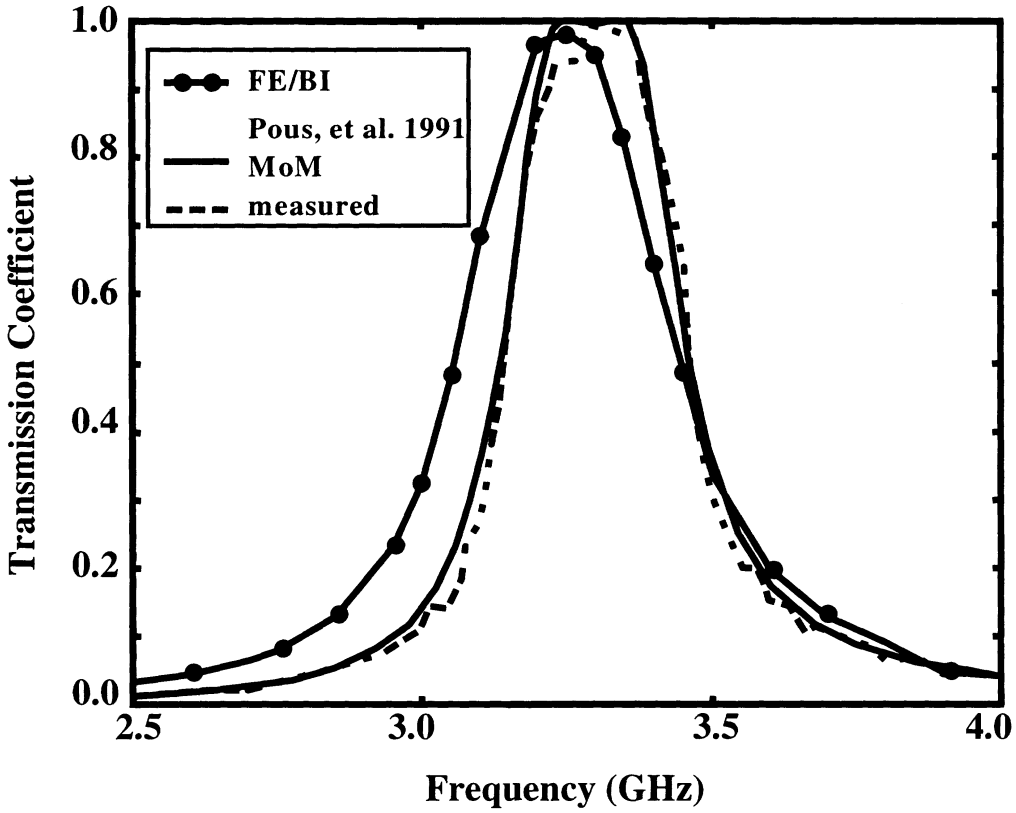

Figure 9: Transmission coefficient for the FSS structure in Fig. 7 compared to reference values from [2], $L_s = 9$ mm: FE/BI ($L_s = 8$ mm: Reference), $W_s = 2$ mm, $W_p = 28$ mm, $L_p = 28$ mm, (TM, $\vartheta_0 = 0.1^o, \varphi_0 = 0^o$).

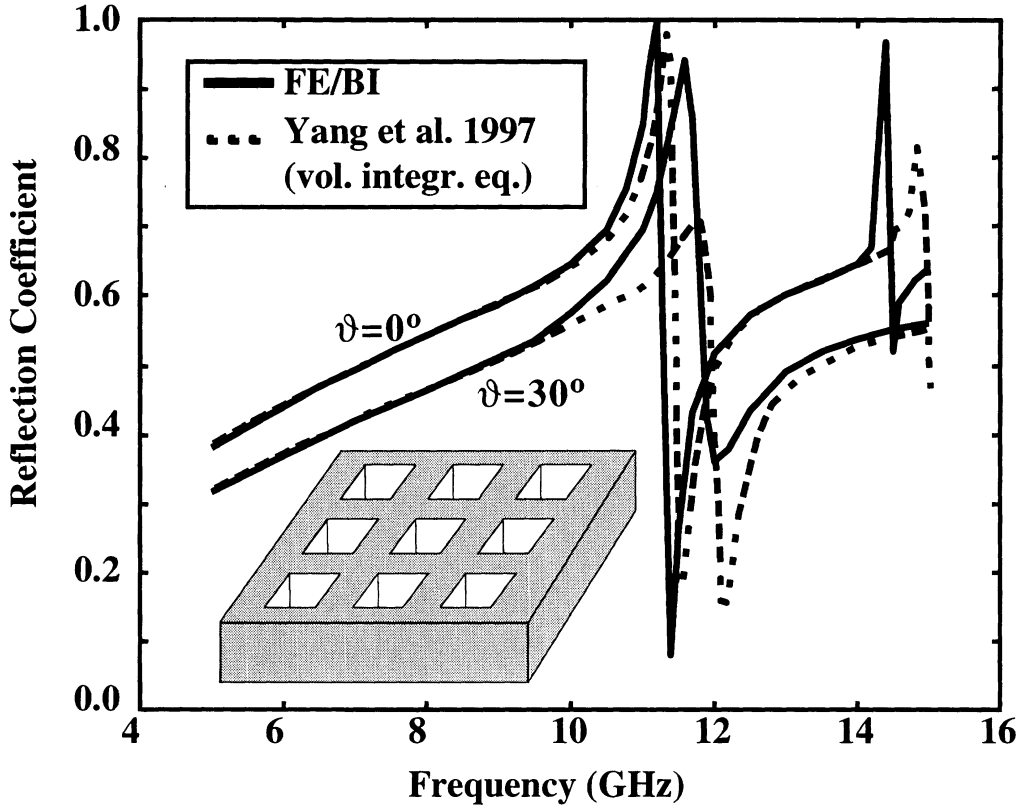

Figure 10: Plane wave reflection from a dielectric slab ($\varepsilon_r = 4$) with planarly embedded periodic material blocks ($\varepsilon_r = 10$) compared to reference values from [11], Slab height: 0.2 cm, period: 2×2 cm, block side length: 1×1 cm (TM, $\vartheta_0 = 0.1^o, \varphi_0 = 0^o$)

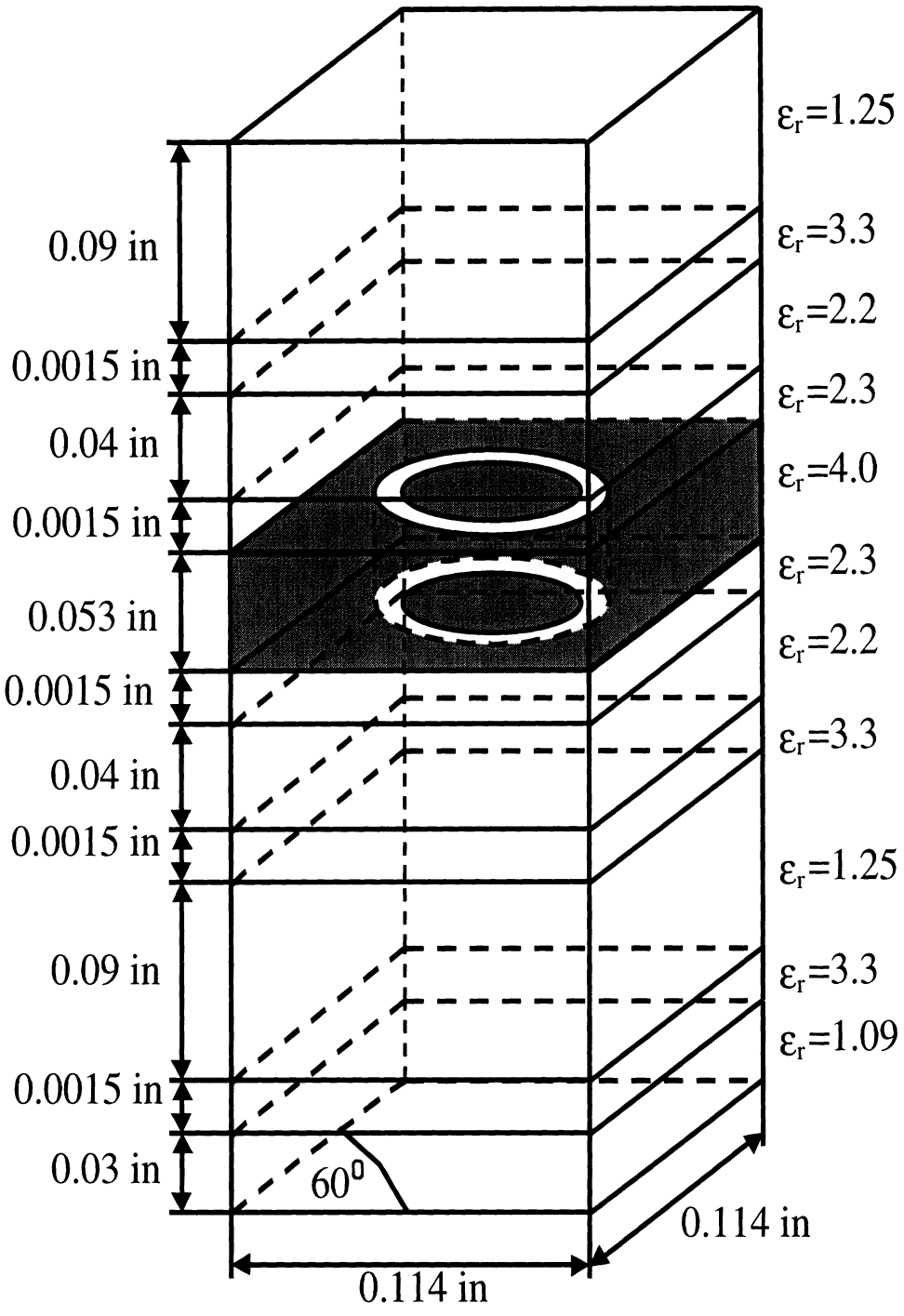

Figure 11: Unit cell of "artificial puck plate" FSS as presented in [13].

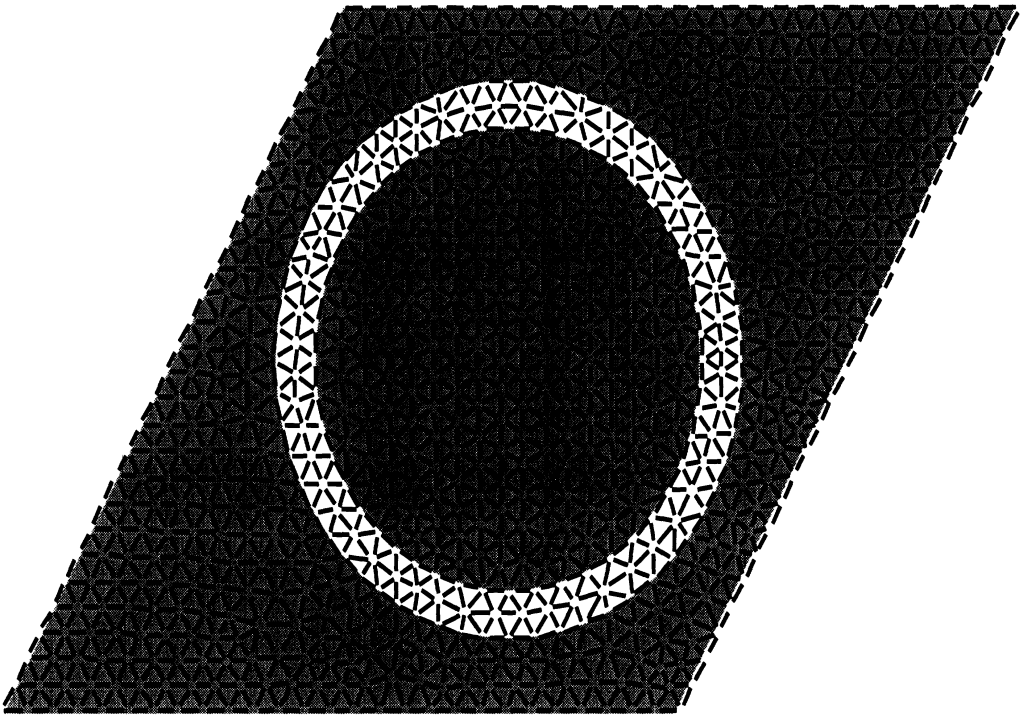

Figure 12: Triangular surface mesh for the structure in Fig. 11

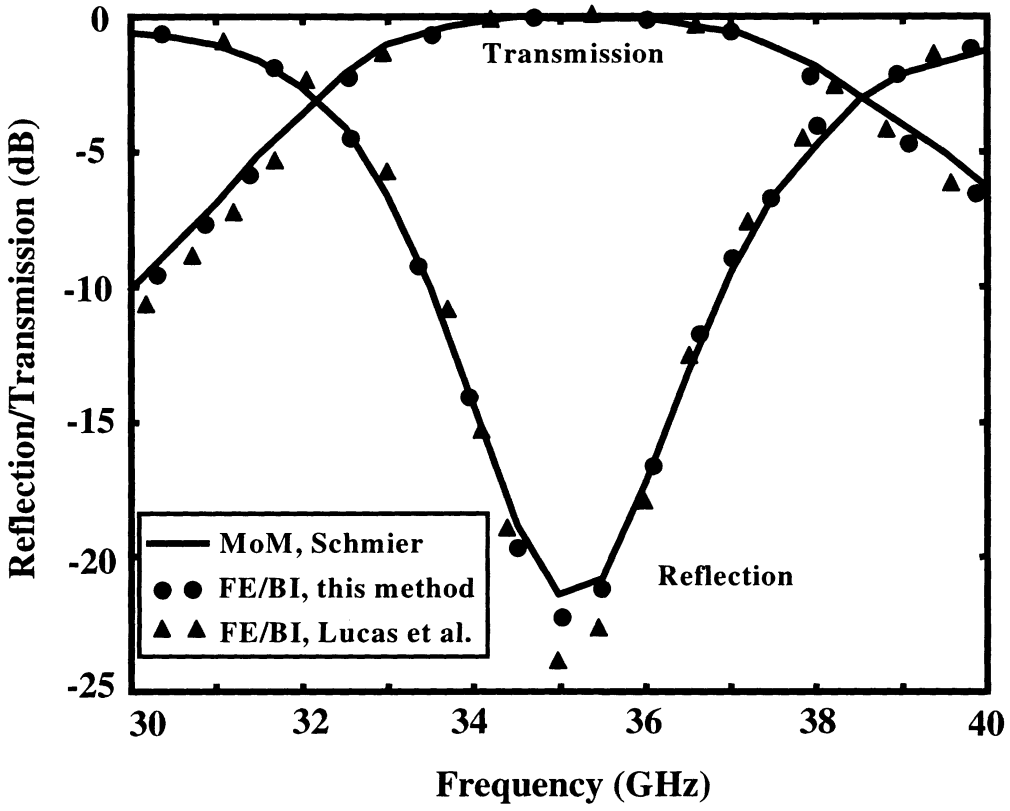

Figure 13: Reflection and transmission coefficients for bandpass structure in Fig. 11 compared to reference values from [13], (TE, $\vartheta_0 = 0.1^o, \varphi_0 = 0^o$).